PAPER

Activating earth-abundant electrocatalysts for efficient, low-cost hydrogen evolution/oxidation: sub-monolayer platinum coatings on titanium tungsten carbide nanoparticles†

Sean T. Hunt, Maria Milina, Zhenshu Wang and Yuriy Román-Leshkov*

Most earth-abundant electrocatalysts suffer from negligible activity for the hydrogen oxidation reaction (HOR) and significant overpotentials for the hydrogen evolution reaction (HER) in acidic media. We designed earth-abundant, carbon-supported titanium tungsten carbide ($Ti_xW_{1-x}C$) nanoparticles decorated with surface Pt coatings ranging from the "single-atom" to the two-monolayer regime. Reactivity studies demonstrated that sub-monolayer Pt coverages are optimal and could activate the exposed metal carbide sites for both HER and HOR at low overpotentials. Specifically, a 0.25 monolayer coverage of Pt improved the exchange current density of $Ti_{0.2}W_{0.8}C$ by more than three orders of magnitude. This catalyst outperformed traditional Pt/C by a factor of 13 on a Pt mass basis, allowing for over a 96% reduction in Pt loadings. Deactivation was not observed after 10 000 cycles between −50 and +600 mV *vs.* RHE in 1.0 M $HClO_4$, and activity was maintained after 140 000 catalytic turnovers. A technoeconomic analysis revealed that over the catalyst lifetime, this new architecture could reduce materials and energy costs by a factor of 6 compared to state-of-the-art earth-abundant catalysts and a factor of 12 compared to Pt/C.

Broader context

The noble metals are nature's universal catalysts, but are scarce and expensive resources. Core–shell nanoparticles, comprised of an inexpensive and earth-abundant core with an atomically-thin monolayer noble metal shell offer a new direction for the design of highly active and stable catalysts with reduced noble metal loadings. Here, we show that sub-monolayer surface coverages can offer even further loading reductions (over 96%) while also exposing and activating the earth-abundant core for active co-catalysis. The advantages of this catalyst architecture are demonstrated using sub-monolayer Pt decorations on bimetallic titanium tungsten carbide (TiWC) core nanoparticles for both hydrogen evolution and hydrogen oxidation reactions in acidic media. A technoeconomic analysis shows that this catalyst architecture results in the lowest-cost HER/HOR catalyst designed to date, with activity and stability comparable to commercial Pt catalysts, while containing negligible noble metal loadings.

Introduction

A future global hydrogen economy critically depends on two key technologies: water electrolyzers and fuel cells.[1] Water electrolyzers store energy generated from renewable sources (*e.g.* wind and solar) into hydrogen bonds *via* the hydrogen evolution reaction (HER) at the cathode and the oxygen evolution reaction (OER) at the anode. Fuel cells then provide on-demand power to end-users by the hydrogen oxidation reaction (HOR) at the anode and the oxygen reduction reaction (ORR) at the cathode. Traditionally, noble metal (NM) nanomaterials are the most

active and stable catalysts for all four reactions. However, the high cost and scarcity of the NMs has spawned an intense global research effort into the development of earth-abundant and inexpensive alternatives, especially when considering that the traditional NM nanomaterials remain susceptible to dissolution, sintering, leaching, and support degradation deactivation mechanisms.[2–4] Although impressive progress has been made in the development of earth-abundant catalysts that match or outperform NMs for each reaction in alkaline media,[5–8] acidic media is still preferred in these devices due to faster overall kinetics and the proliferation of inexpensive and efficient Nafion proton exchange membranes.[9–11]

However, designing active and earth-abundant catalysts that are stable above 0 V *vs.* RHE remains challenging in acidic media. Despite the development of a significant number of

Department of Chemical Engineering, Massachusetts Institute of Technology, Cambridge, MA, 02139, USA. E-mail: yroman@mit.edu

3290 | *Energy Environ. Sci.,* 2016, **9**, 3290–3301

This journal is © The Royal Society of Chemistry 2016

alternative catalysts for HER, most notably transition metal sulfides and phosphides,[12–16] NM-based catalysts are still the preferred catalysts for HOR, ORR, and OER.[5,17–19] In the case of HER and HOR, the activity and stability of Pt is unparalleled. For instance, commercial carbon-supported Pt catalyst (Pt/C) is so active that its intrinsic kinetics cannot be measured with rotating disk electrodes (RDEs), instead requiring gas diffusion electrodes (GDEs) or H_2 pump experiments.[17,18,20] For both HER and HOR, Pt outperforms other highly active metals, such as Rh and Pd by a factor of 20 and 40, respectively.[20] As such, state-of-the-art earth-abundant catalysts remain significantly less active for HER than Pt/C. Critically, these earth-abundant catalysts also have poor anodic stability and exhibit negligible HOR activity, an arguably more commercially relevant reaction than HER.

Core–shell nanostructures have emerged as a promising architecture to exploit the remarkable activity, stability, and versatility of Pt, while decreasing overall NM loadings.[21] Early transition metal carbides (TMCs), in particular tungsten carbide (WC), have been proposed as ideal core candidates for supporting Pt.[22–24] WC is earth-abundant, inexpensive, and exhibits a "Pt-like" electronic density of states (DOS). In addition, WC-based nanoparticles have demonstrated stability up to +600 mV vs. RHE over thousands of cycles, making them viable candidates for applications in HOR.[25] Other carbides, such as TiC, TaC, and ZrC have been shown to be even more stable than WC.[26] Despite their lower activity, alloying more stable carbides, such as TaC, with WC can produce a more anodically stable catalyst without sacrificing catalytic activity.[27] Although model thin film studies of Pt and Pd monolayers (MLs) on WC and Mo_2C have indicated that a ML coverage is enough to achieve the HER activity of bulk Pt or Pd thin films, HOR performance was not explicitly addressed in these experiments.[28–30] To date, these exciting results have not been translated into nanoparticle-based systems.

In the present study, we bridge the materials gap between the thin film results and a true high surface area nanoparticle formulation by using a synthesis method recently developed in our group to generate core–shell TMC nanoparticles coated with thin NM shells.[24] In this method, mixtures of NM salts and transition metal oxides encapsulated in removable silica templates self-assemble into core–shell nanostructures during high-temperature carburization, resulting in a highly active, stable, and tunable catalytic platform. In contrast with the thin film studies, we establish that on the nanoscale, only sub-monolayer coverages on the TMC cores are needed to approach the activity of state-of-the-art Pt/C commercial catalysts. A kinetic analysis indicates that the TiWC core is activated by sub-monolayer Pt coverages to participate in both HER and HOR, greatly boosting the overall performance of the material. The optimal catalyst was observed to be stable over thousands of cycles up to +600 mV. Finally, a technoeconomic analysis reveals that sub-monolayer core–shell nanoparticles achieve the best tradeoff between operating overpotential and Pt loading, resulting in an inexpensive and stable catalyst for both water electrolyzer cathodes and fuel cell anodes operating in acidic media. Such an active and inexpensive catalytic system capable of efficient HER and HOR could aid in further reducing the costs of unitized regenerative fuel cells (URFCs).[31]

Experimental section

Synthesis of supported TiWC, Pt/TiWC, and Pt catalysts

Transition metal carbide nanoparticles with or without Pt coatings were prepared using a reverse microemulsion (RME) method reported in detail elsewhere.[24,25,32] Briefly, 240 mL of n-heptane, 54 mL of Brij-L4® surfactant, 7.8 mL of ultrapure deionized (DI) water, and 1.4 mL of NH_4OH solution were mixed under constant stirring resulting in an optically transparent and colorless RME. Tungsten and titanium isopropoxides (1.1 mmol total) were mixed in the desired ratio, diluted with 120 mL of n-heptane, and then added to the RME over the span of a few minutes under ambient conditions (i.e. without using a Schlenk line). The RME was allowed to react under constant mixing for 4 h to form bimetallic transition metal oxide (TMO) nanoparticles (NPs). For Pt-coated NPs, a separate RME consisting of 46 mL of n-heptane, 7.2 mL of Brij-L4® surfactant, and 1 mL of an aqueous solution of chloroplatinic acid in the desired concentration (0.1–40 mg mL^{-1}) was then added to the original RME dropwise over the span of ~30 min and left to mix for an additional 4 h. Next, 1.5 mL of tetraethyl orthosilicate (TEOS) was rapidly injected and allowed to react for 16.5 h. Finally, 300 mL of methanol was added to the RME to precipitate the resulting silica-encapsulated TMO or $PtCl_x$/TMO NPs, which were recovered after flocculation, sedimentation, decanting, centrifugation, and washing with acetone.

Collected solids were dried at room temperature under vacuum and carburized at 900 °C (heating ramp of 2 °C min^{-1}) in a flow of H_2 (130 cm^3-STP min^{-1}) and CH_4 (23 cm^3-STP min^{-1}) for 4.5 h followed by a 30 min treatment at 900 °C in a H_2 flow (130 cm^3-STP min^{-1}). Ultra-high purity (UHP) gases were used for all treatments. After cooling to room temperature in H_2, the materials were passivated with an H_2O-saturated N_2 flow (100 cm^3-STP min^{-1}) for 2 h and then with a 1%O_2/99%N_2 mixture (100 cm^3-STP min^{-1}) for the same amount of time. To remove the encapsulating SiO_2 shells and to support the NPs on carbon black, a well-mixed solution of 10 mL of degassed ethanol and 200 μL of reagent-grade 48 weight percent (wt%) aqueous HF was added to ~60 mg of SiO_2/TiWC or SiO_2/Pt/TiWC NPs and ~20 mg of carbon black (Vulcan® XC-72r, Cabot) and left to react for 18 h at room temperature and constant mixing using an orbital shaker. The resulting catalysts were recovered by centrifugation and washed thoroughly with degassed ethanol and water. The powders were dried under vacuum and stored in a dry N_2 glovebox.

A 0.15 wt% Pt/C control catalyst was synthesized by vigorously mixing 657 μL of a 575 μg mL^{-1} solution of chloroplatinic acid in DI water with 99.4 mg of dried Vulcan® XC-72 carbon black over 1 h. The mixture was dried in air at 120 °C and subsequently reduced by holding at 300 °C for 2 h in 100 cm^3-STP min^{-1} H_2 using a 2 °C min^{-1} ramp rate.[33] Commercial 20 wt% Pt/C catalyst supported on Vulcan® XC-72 was supplied by Premetek (Wilmington, DE).

This journal is © The Royal Society of Chemistry 2016

Energy Environ. Sci., 2016, 9, 3290–3301 | 3291

Materials characterization

Powder X-ray Diffraction (PXRD) patterns were collected on a Bruker D8 diffractometer using Cu Kα radiation. Data were recorded in the range of 15–90° 2θ with an angular step size of 0.01° and a counting time of 0.1 s per step. X-ray Photoelectron Spectroscopy (XPS) was performed on a PHI Versaprobe II equipped with a multichannel hemispherical analyzer and a monochromatic aluminum anode X-ray source operating at 100 W with a 100 μm beam scanned over a 1.4 mm line across the sample surface. A dual-beam charge neutralization system was used with an electron neutralized bias of 1.2 eV and an argon ion beam energy of 10 eV. All spectra were charge corrected by referencing the adventitious C 1s signal to 284.7 eV. Samples were prepared by evaporating nanoparticle dispersions in DI water onto electrically conductive copper tape. Transmission Electron Microscopy (TEM) was performed on a JEOL 2010F equipped with a field emission gun (FEG) operating at 200 kV. Scanning electron microscopy (SEM) was performed with a Zeiss Merlin High-resolution SEM operating at 1 kV.

Chemical composition of the NPs was determined using Inductively Coupled Plasma Mass Spectrometry (ICP-MS), performed on an Agilent 7900 ICP-MS. The silica-encapsulated unsupported NPs were digested using a mixture of HCl–HNO₃–HF. Two methods were used to determine the Pt loadings on the electrodes. In Method 1, the wt% Pt of the carbon-supported catalyst was determined by ICP-MS after catalyst digestion in aqua regia followed by filtration and dilution in 2 vol% HNO₃. This method was benchmarked against total wt% loading determination using thermogravimetric analysis (TGA), performed on a Q500 thermal analysis system (TA Instruments) between 25 and 800 °C (with 15 min isothermal hold at 150 °C) using a heating ramp of 5 °C min⁻¹ under 45 cm³-STP min⁻¹ of air and 5 cm³-STP min⁻¹ of N₂ flow. They were found to be within 1% agreement. The wt% loadings of Pt on the electrodes were then calculated based on the ink concentrations. In Method 2, triplicate electrode mountings were fully submerged in separate vials of aqua regia overnight, diluted with 2 vol% HNO₃, and then subjected to ICP-MS analysis to determine wt% loadings. The error in Pt loadings between different electrode mountings was found to be less than 2%. The two methods were found to be within 5% agreement. For instance, the 0.25 ML Pt/TiWC/C sample was loaded onto the electrode at 2.05 ± 0.06 μg_{Pt} cm$_{geo}^{-2}$ determined by Method 2, while the loading was calculated to be 2.13 μg_{Pt} cm$_{geo}^{-2}$ using Method 1. All Pt loadings reported here were determined by Method 2 as direct electrode digestion was deemed more accurate. The only exception is the <0.01 ML sample where the Pt loading was so low that direct digestion of the electrode could not be used and instead Method 1 was applied.

Electrochemical study

Electrochemical measurements were performed on a CH Instruments 627e potentiostat/galvanostat using a jacketed glass cell with PTFE cap and gas diffusion electrodes (GDEs).[17,18] A platinized platinum coil was used as the counter electrode for initial activity measurements. A graphite rod (99.9995%) was used as the counter electrode for all stability measurements to prevent the long-term contamination of the working electrode with cathodically deposited Pt, a common problem in the literature.[34] A leak-proof 3 M NaCl Ag/AgCl electrode calibrated to an eDAQ hydrogen electrode was employed as the reference electrode. All potentials are reported *vs.* RHE. Catalyst inks were prepared at the concentration of 3 mg of catalyst per gram of solution by dispersing the carbon-supported materials in a mixture of water, isopropanol, ethanol, (H₂O : IPA : EtOH = 25 : 50 : 25) and 5% Nafion® 117 (18 μL per 3 mg of catalyst). The inks were sonicated for 1 h in an ice bath. Carbon paper (Sigracet GDL 25 BC from fuelcellstore.com) was used to prepare the GDEs. The carbon paper was cut into 1 × 2 cm strips and 17 μL of ink was applied to a 0.2 × 1 cm line at one end of the GDE.[17] The ink was left to dry vertically in ambient conditions for 2 min and under vacuum for 5 min. For the control catalysts, the NM loading was ∼51 μg cm$_{geo}^{-2}$ while for the core–shell catalysts, the NM loading ranged from ∼20 μg cm$_{geo}^{-2}$ to ∼0.03 μg cm$_{geo}^{-2}$. Exact loadings were determined using electrode digestion followed by ICP-MS (*vide supra*).

The GDE was then suspended vertically in 1.0 M HClO₄ solution at 30 °C using a freshly-polished Ti wire. The solution level was maintained such that the bottom 0.4 cm of the GDE was submerged in solution. In this configuration, the uncompensated solution resistance was ∼4 Ω. The bubbler was not positioned in the electrolyte solution but rather directly above the solution and maintained with 300 cm³-STP min⁻¹ of either UHP Ar or UHP H₂. Once submerged, the GDE was cycled from 0 V to 0.6 V at 200 mV s⁻¹ in Ar-purged 0.1 M HClO₄ at 30 °C for 100 conditioning scans. The electrolyte was refreshed, and the flow was then switched to H₂ and two uncompensated LSV scans were obtained at 10 mV s⁻¹. The first was from 150 mV to −150 mV, and the second from −150 mV to 150 mV. The average of these two scans was taken for each electrode mounting.[17] The LSV scans were then repeated with instrument-applied 90% iR compensation. An additional kinetic study was performed on the optimal catalyst by measuring iR-compensated LSVs at 7 different temperatures. The jacketed cell was equilibrated at each temperature for 10 min after the setpoint was reached. Two stability studies were conducted on the optimal catalyst. The first involved 10 000 cycles between −50 mV and +600 mV at 100 mV s⁻¹ in Ar-saturated 1.0 M HClO₄. The second stability study was performed in H₂-saturated 1.0 M HClO₄ using chronopotentiometry (CP) by cycling between 5 mA cm$_{geo}^{-2}$ of HOR for 15 min followed by −5 mA cm$_{geo}^{-2}$ of HER for 15 min and continuing for 16 h on stream.

Results and discussion

Design of Pt/TiWC catalysts

Recently, our group developed a new method to generate TMC nanoparticle cores coated with NM shells with full control over the average particle size, the core composition, and the shell composition.[24] This method enables the translation of thin film studies of Pt/WC into a high surface area nanoparticle

formulation. In the present study, we use TiWC cores for added anodic stability, with core compositions ranging from $Ti_{0.1}W_{0.9}C$ to $Ti_{0.2}W_{0.8}C$. By varying the amount of Pt, we were able to tune the ML coverage from the regime of atomically-dispersed Pt atoms to ca. 2–3 monolayers (MLs).

Careful consideration was given to define the appropriate particle size regimes that should be investigated for the various ML coverages (Fig. S1, ESI†). We determined that 4 nm particle sizes represent a soft cutoff between "sub-ML efficient" and "ML efficient" catalyst designs. This cutoff was calculated using particle size as a control variable and minimizing an objective function comprised of the ratio of surface atoms to bulk atoms and the total atoms in the nanoparticle. These quantities were chosen to construct the objective function because the design goal is to minimize Pt loadings. Intuitively, the ratio of surface atoms to bulk atoms must be minimized to ensure low Pt loadings. In the case of a 1 nm nanoparticle, more than 50% of the atoms reside at the surface (Fig. S1, ESI†). As such, synthesizing 1 nm Pt/TiWC core–shell nanoparticles with complete ML coverages would not offer substantial Pt loading reductions. Only nanoparticles larger than ca. 4 nm offer significant Pt loading reductions at ML and multilayer coverages. Minimization of total atoms in the nanoparticle prevents the optimization tending towards large nanoparticles with single ML coverages but small real surface areas.

Sample nomenclatures were chosen based on the calculated ML coverage, which was computed from the TEM-determined average particle dispersion and the ICP-MS-determined Pt : TiW molar ratio (Table 1). Fig. 1 and Fig. S2 (ESI†) depict representative TEM images of the materials as well as an SEM image of the 2 ML sample showing its dispersion to a greater depth of field. The surface dispersion was calculated based on standard methods assuming spherical particles and complete phase-separation of Pt from the TiWC core. For example, the 0.25 ML Pt/TiWC sample has an average particle size of 3.1 nm and a Pt : TiW ratio of 4%. By calculation, this corresponds to a 0.25 ML surface coverage assuming Pt fully partitions to the TiWC surface during synthesis.

Table 1 Chemical composition and particle size distribution

Sample[a]	Ti : W[b] (mol%)	PSD[c] (nm)	PSD[d] (nm)	Pt : TiW[e] (mol%)	Pt[f] (wt%)
TiWC	10	3.0 ± 1.1	3.1	—	0
<0.01 ML Pt/TiWC	20	3.2 ± 0.9	2.9	0.05	0.014
0.05 ML Pt/TiWC	20	2.9 ± 0.9	3.0	0.7	0.15
0.25 ML Pt/TiWC	20	3.1 ± 0.9	2.7	4	0.72
0.75 ML Pt/TiWC	20	3.8 ± 0.9	2.8	11	2.5
2 ML Pt/TiWC	10	7.7 ± 1.4	5.0	28	8
20 wt% Pt/C	—	1.4 ± 0.3	1.9	—	20
0.15 wt% Pt/C[g]	—	~3–4	—	—	0.15

[a] All samples are supported on Vulcan XC-72r at ca. 20 wt% (total metals basis), with the exception of 0.15 wt% Pt/C. [b] Ti : W molar ratio determined by ICP. [c] Derived from TEM based on at least 200 NPs. [d] Derived from PXRD patterns using the Scherrer equation. [e] Pt : TiWC molar ratio determined by ICP. [f] Pt loading for supported catalysts determined by ICP. [g] Due to the low loading, PSD for 0.15 wt% Pt/C could only be estimated from TEM using a smaller number of NPs, while the intensity of the PXRD signal was insufficient for the calculations.

Catalyst structure characterization

The catalyst structure was interrogated by combining PXRD and TEM measurements with comparisons of XPS-determined surface compositions to ICP-determined bulk compositions. Fig. 2a depicts wide angle X-ray diffractograms of the nanoparticles supported on carbon black. The commercial Pt catalyst consists of 1.4 ± 0.3 nm NPs dispersed at 20 wt% on a Vulcan XC-72r support (Fig. S2, ESI†) and displayed broad reflections at 39.9°, 46.2°, 67.8°, and 81.2°. These reflections are consistent with the 111, 200, 220, and 311 planes of phase-pure fcc Pt, respectively. In contrast, the core–shell nanoparticles as well as the TiWC control only exhibit reflections centered around 37.0°, 42.9°, 62.5°, 74.9°, and 79.0°, consistent with the 111, 200, 220, 311, and 222 planes of phase-pure fcc β-WC, respectively. Even 2 ML Pt/TiWC, which contains 28 mol% Pt, does not show indications of a separate, discrete fcc Pt phase. These diffractograms are consistent with Pt shells lattice-matched to the TiWC core. The peak broadening is in agreement with the particle size distributions (PSDs) derived from the TEM analysis (Table 1). Namely, the PSDs for carbon-supported TiWC, 0.004 ML Pt/TiWC (denoted as <0.01 ML Pt/TiWC), 0.05 ML Pt/TiWC, and 0.25 ML Pt/TiWC are ca. 3.0 ± 1.0 nm while those of 0.75 ML and 2 ML Pt/TiWC are 3.8 ± 0.9 nm and 7.7 ± 1.4 nm, respectively.

In Fig. 2b, XPS spectra are shown for representative core–shell nanoparticles formulated as unsupported nanopowders in order to afford the maximum signal intensity of the metal peaks. The 2 ML sample displays a clear and intense Pt 4f signal centered at 71.5 eV and 74.9 eV, consistent with Pt^0. Deconvolution of the Pt 4f signal (not shown) demonstrates a substantial signal contribution from signals centered around 72.6 eV and 76 eV, consistent with a Pt^{2+} passivation layer. The $Pt^{2+} : Pt^0$ ratio of 0.3 is in agreement with a 2–3 ML shell. Importantly, the 0.25 ML sample shows only two Pt^{2+} peaks, centered around 72.3 eV and 75.7 eV. Because Pt natively passivates with a PtO layer, the lack of a detectable Pt^0 signal implies the near-complete Pt dispersion associated with sub-monolayer coverages. The downward core-level shift in the Pt^{2+} peak location from the 2 ML sample also implies immediate interaction with the TiWC substrate. The 0.05 ML and <0.01 ML samples could not be quantitated due to the extremely low Pt coverages. Despite the low signal intensity, the 0.05 ML sample appears to be composed of Pt^{2+} as well as a second Pt^{x+} species in a chemical environment that is intermediate between Pt^{2+} and Pt^{4+} (an amplified spectrum shown in Fig. S3, ESI†). The peak locations are ca. 73.2 and 76.5 eV for the Pt $4f_{7/2}$ and $4f_{5/2}$ peaks, respectively. The surface Pt concentration in the <0.01 ML sample exceeds the instrument detection limits and as such is "XPS-invisible."

Comparison of the XPS-determined surface composition with the ICP-determined bulk composition (Table 1) evidences the core–shell structure of the 2 ML and 0.25 ML samples for which the Pt 4f signals are quantifiable in the XPS spectra. In a radially isotropic heterometallic nanoparticle, the XPS-determined surface composition will agree with the ICP-determined overall composition. However, in a core–shell nanoparticle, the species
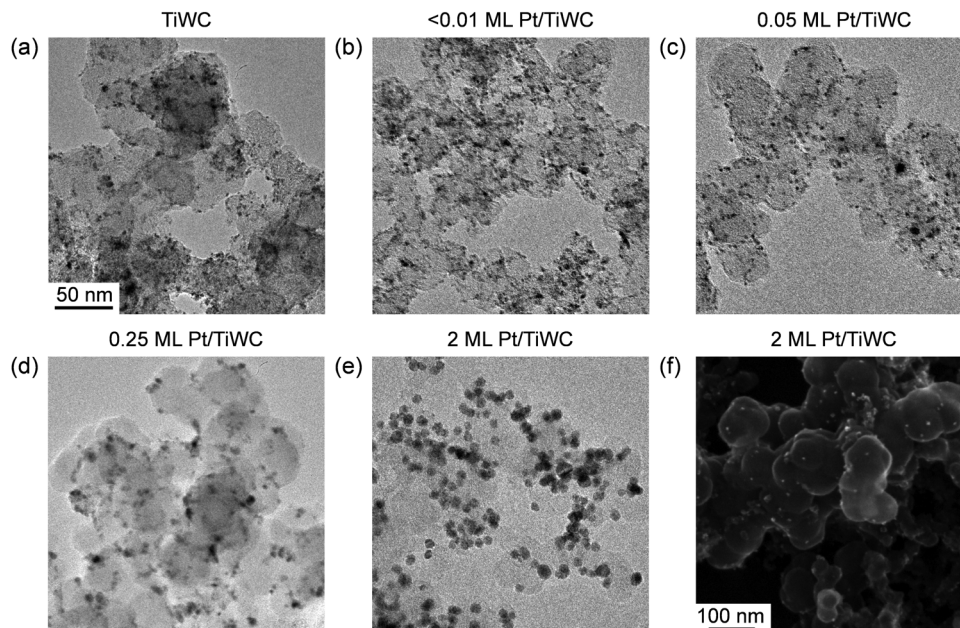
This journal is © The Royal Society of Chemistry 2016

Energy Environ. Sci., 2016, **9**, 3290–3301 | **3293**

Fig. 1 Transmission electron micrographs of carbon-supported (a) TiWC, (b) <0.01 ML Pt/TiWC, (c) 0.05 ML Pt/TiWC, (d) 0.25 ML Pt/TiWC and (e) 2 ML Pt/TiWC. The scale bar shown in (a) applies to all micrographs from (a) to (e). (f) Scanning electron micrograph of 2 ML Pt/TiWC.
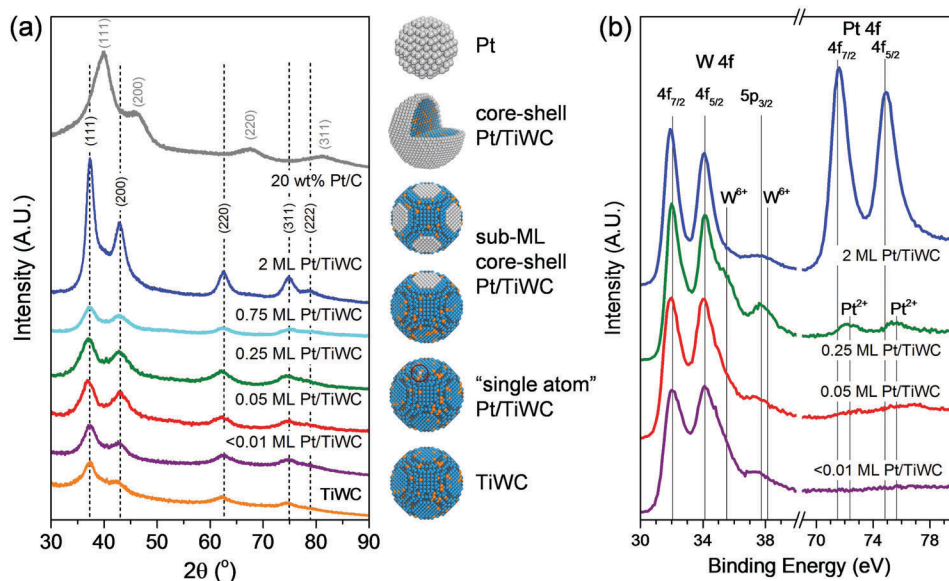

Fig. 2 (a) X-ray diffraction patterns of supported catalysts and (b) representative XPS spectra of nanodispersions after silica dissolution for W and Pt signals.

that is enriched at the surface screens the XPS signal of the sub-surface elements, resulting in a difference between the XPS-determined surface and the ICP-determined bulk compositions.[24] The extent of the surface enrichment is directly related to the ML coverage, with thicker shells exhibiting a higher enrichment relative to sub-monolayer coverages. In the case of the 2 ML sample, the ICP-determined overall ratio of Pt:W was 28%. However, the XPS-determined ratio of Pt:W was 49%, indicative of extensive screening of the core by the Pt shell. Similarly, the ICP-determined ratio of Pt:W in the 0.25 ML sample was 4%

while the XPS-determined ratio of Pt:W was 11%, again indicative of Pt screening the W signal.

While the XPS signal was too low for the 0.05 ML and <0.01 ML samples to examine screening effects, their ML coverage was estimated from a combination of TEM-determined PSDs and ICP-determined overall compositions. We note that the Pt concentration in the <0.01 ML sample is so low that the average 3 nm TiWC NP would have a surface coverage of 0.6 Pt atoms, meaning that this sample, on average, approaches the level of a single Pt atom decorating a TiWC nanoparticle. By calculation,

3294 | *Energy Environ. Sci.*, 2016, **9**, 3290–3301

This journal is © The Royal Society of Chemistry 2016

this value would correspond to a surface coverage of *ca.* 0.004 ML, which is consistent with the undetectable XPS signal shown for this sample in Fig. 2b. We also note that while scanning-transmission electron microscopy–energy dispersive X-ray spectroscopy (STEM–EDX) mapping is the most direct method for examining core–shell structures (Fig. S4, ESI†),[24] it could not readily be applied to sub-monolayer or single-atom configurations due to the inherently low Pt signal intensities and the similar *Z*-contrast between Pt and W. As such, we do not have conclusive proof of single atom dispersion, and cannot rule out the existence of small Pt clusters that are also undetectable by XPS. Similarly, the sub-monolayer configuration graphics are proposed representations of how Pt could arrange on the TiWC nanoparticle at these low coverages.

HER and HOR electrochemical activity measurements

Employing gas diffusion electrodes (GDEs) in 1.0 M HClO$_4$ under an H$_2$ partial pressure of 101.3 kPa, the materials were examined for both HER and HOR using linear sweep voltammetry (LSV) at 10 mV s^{-1} at 30 °C. The exact Pt loading on each electrode was determined by digestion of the GDEs in aqua regia, performed in triplicates as described in the Experimental section. The Pt loadings used to normalize each electrode were determined to be as follows: 51 μg$_{Pt}$ cm$_{geo}$$^{-2}$ for the commercial 20 wt% Pt/C, 20 μg$_{Pt}$ cm$_{geo}$$^{-2}$ for 2 ML Pt/TiWC, 6.5 μg$_{Pt}$ cm$_{geo}$$^{-2}$

for 0.75 ML Pt/TiWC, 2.1 μg$_{Pt}$ cm$_{geo}$$^{-2}$ for 0.25 ML Pt/TiWC, 0.42 μg$_{Pt}$ cm$_{geo}$$^{-2}$ for 0.05 ML Pt/TiWC, 0.38 μg$_{Pt}$ cm$_{geo}$$^{-2}$ for the 0.15 wt% Pt/C control, and 0.03 μg$_{Pt}$ cm$_{geo}$$^{-2}$ for <0.01 ML Pt/TiWC.

Fig. 3a depicts the LSVs obtained for each material over a large potential window to show the activity of unmodified TiWC/C, the 0.15 wt% Pt/C control, and <0.01 ML Pt/TiWC. Each of these catalysts has negligible HOR activity. Remarkably, the <0.01 ML Pt/TiWC outperforms the 0.15 wt% Pt/C control for HER despite more than an order of magnitude reduction in loaded Pt. The other catalysts are so active for both HER and HOR that they appear as nearly vertical lines at the given scale.

When the LSVs presented in Fig. 3a are plotted over a narrower potential range but broader current range (Fig. 3b), it can be seen that 2 ML Pt/TiWC is actually more active than the commercial 20 wt% Pt/C catalyst, despite a factor of 2.5 reduction in Pt loading. This result suggests that the TiWC core favorably modifies the electrochemical activity of Pt towards HER. DFT calculations have revealed a more favorable hydrogen binding energy (HBE) on Pt/WC in comparison to native Pt. While this effect did not translate into a measureable activity improvement in previous model thin film studies,[28] here we see a significant activity enhancement for Pt/TiWC nanoparticle formulations.

As shown in Fig. 3c, the data (re-expressed as a semilog plot typical for Tafel analyses) demonstrates that the 0.05 ML
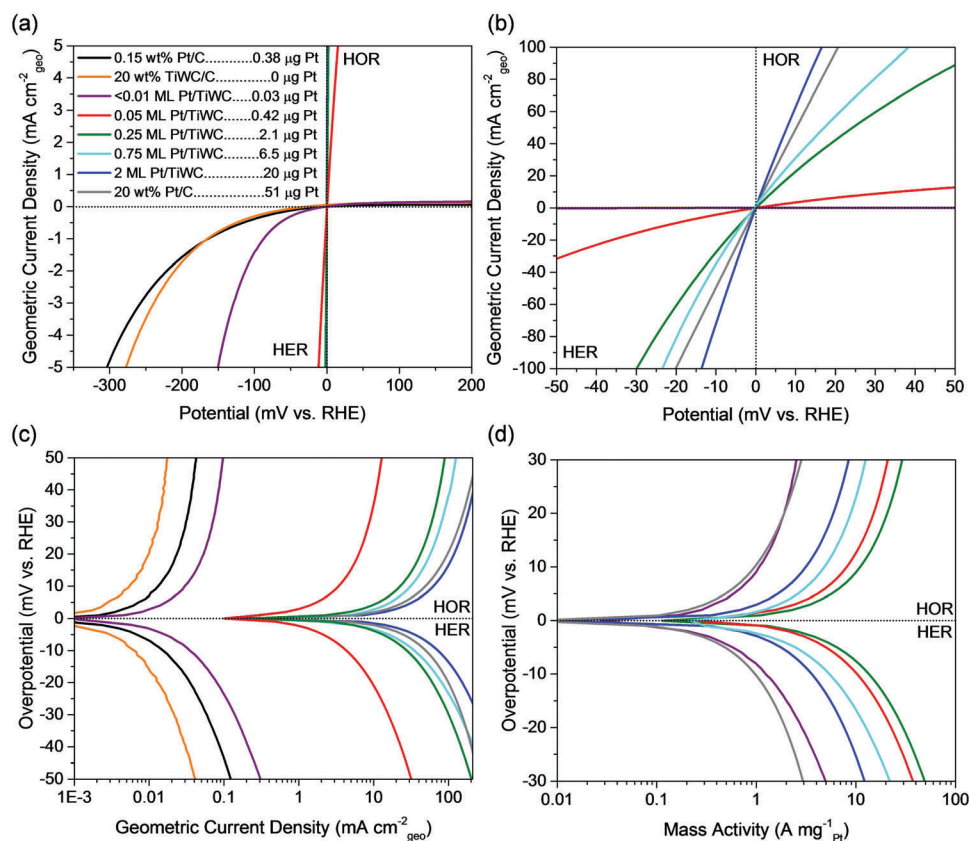

Fig. 3 (a and b) LSVs and (c and d) Tafel plots obtained for supported catalysts in 1.0 M HClO$_4$ at 10 mV s^{-1} at 30 °C. The legend shown in (a) applies to (b–d). All materials were loaded at the same total mass per geometric surface area (255 μg$_{cat}$ cm$_{geo}$$^{-2}$); the masses listed in (a) refer to the geometric Pt mass loadings for each catalyst and apply to (b–d).

This journal is © The Royal Society of Chemistry 2016

Energy Environ. Sci., 2016, **9**, 3290–3301 | **3295**

Pt/TiWC catalyst achieves a nearly 2 order of magnitude improvement in current density compared to the unmodified TiWC control. Furthermore, despite both the 0.05 ML Pt/TiWC catalyst and the 0.15 wt% Pt/C control having similar Pt loadings ($\sim$0.4 μg_{Pt} cm$_{geo}^{-2}$) the 0.05 ML Pt/TiWC catalyst is over two orders of magnitude more active than the control.

Although comparing the reactivity normalized by the number of surface sites using electrochemical active surface area (ECSA) measurements is preferred, we found that the extremely low concentrations of Pt in 0.25 ML Pt/TiWC, 0.05 ML Pt/TiWC, and <0.01 ML Pt/TiWC samples made them unsusceptible to CO stripping. Thus, normalization of the activity by the concentration of surface sites could not be reliably performed. Instead, Pt mass activity was used, which conveniently is the most informative normalization scheme for examining intrinsic improvements in Pt utilization efficiency.

Fig. 3d shows substantial improvements in mass activity for the 0.05 ML, 0.25 ML, and 2 ML samples, with 0.25 ML Pt/TiWC exhibiting the largest enhancement in mass activity.

Kinetic analysis using the Butler–Volmer equation

To quantitate the kinetics of this new class of core–shell catalysts and gain insight into their intrinsic performance, fitting of the LSV data from Fig. 3 was performed over the kinetically limited portions of each data set using the Butler–Volmer equation:

$$j = j_0 \times \left(e^{\frac{\beta_{HOR} F \eta}{RT}} - e^{\frac{-\beta_{HER} F \eta}{RT}} \right)$$

where j_0 is the exchange current density in A cm$_{geo}^{-2}$, β_{HOR} and β_{HER} are the symmetry of charge transfer for HOR and HER, respectively. η is the overpotential in V, R is the ideal gas constant, F is Faraday's constant, and T is the temperature. The fits were performed using a standard nonlinear least squares curve fitting solver package and are shown in Fig. 4a, normalized on a mass basis. The results are summarized both in Table 2 and Fig. 4b.

The commercial 20 wt% Pt/C control exhibits an exceptionally high exchange current density of 117.2 $\pm$ 1.0 mA cm$_{geo}^{-2}$ and near-perfect symmetric charge transfer coefficients of 0.49 and 0.51 for HOR and HER, respectively (Table 2). In contrast, unmodified TiWC displayed an exchange current density of 0.03 mA cm$_{geo}^{-2}$ and highly asymmetric charge transfer coefficients of 0.06 and 0.94 for HOR and HER, respectively. However, as the ML coverage increases, the charge transfer symmetry progressively becomes more symmetric, reaching charge transfer coefficients of β_{HOR} = 0.36 and β_{HER} = 0.64 for the 2 ML Pt/TiWC catalyst. In this respect, the composite Pt/TiWC core–shell catalysts behave as catalytic analogues to Pd and Rh, which natively have charge transfer coefficients of 0.3 and 0.7 for HOR and HER, respectively.[20]

When normalized on a mass basis, the 2 ML Pt/TiWC shows a factor of 3.7 improvement over 20 wt% Pt/C as shown in Fig. 4b. Since 20 wt% Pt/C already consists of ultrasmall nanoparticles with high dispersion, this level of improvement cannot be explained by an increase in the metal dispersion alone, but rather by modification of the electronic structure of Pt by the subsurface TiWC core.
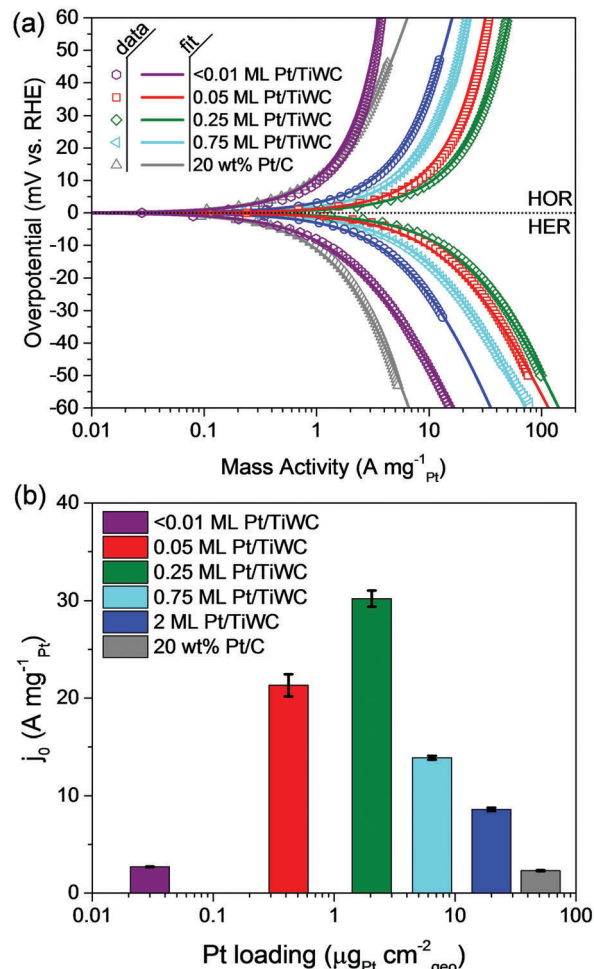

Fig. 4 (a) Tafel plots and their fits to the Butler–Volmer equation obtained in 1.0 M HClO$_4$ at 10 mV s^{-1} at 30 °C. (b) Exchange current density (j_0) derived from the fits vs. Pt loading for supported catalyst.

Table 2 Exchange current densities (j_0) and Tafel slopes (β) derived from the HOR and HER LSVs using nonlinear least squares curve fitting to the Butler–Volmer equation

Sample	j_0 (mA cm$_{geo}^{-2}$)	j_0 (A mg$_{Pt}^{-1}$)	β_{HOR} (—)	β_{HER} (—)
TiWC	0.03 ± 0.00	—	0.06 ± 0.00	0.94 ± 0.00
<0.01 ML Pt/TiWC	0.08 ± 0.00	2.7 ± 0.0	0.17 ± 0.00	0.83 ± 0.00
0.05 ML Pt/TiWC	8.96 ± 0.10	21.3 ± 1.1	0.22 ± 0.00	0.78 ± 0.00
0.25 ML Pt/TiWC	62.0 ± 0.3	30.2 ± 0.8	0.28 ± 0.00	0.72 ± 0.00
0.75 ML Pt/TiWC	90.0 ± 0.5	13.9 ± 0.2	0.24 ± 0.00	0.76 ± 0.00
2 ML Pt/TiWC	172.0 ± 1.0	8.6 ± 0.2	0.36 ± 0.01	0.64 ± 0.01
20 wt% Pt/C	117.2 ± 1.0	2.3 ± 0.1	0.49 ± 0.01	0.51 ± 0.01

Interestingly, as the Pt ML coverage decreases from 2 ML to 0.75 ML, 0.25 ML, and 0.05 ML, surface TiWC sites are increasingly exposed and the mass activity is observed to improve significantly, reaching maximum at 0.25 ML coverage (factor of 13 over the 20 wt% Pt/C catalyst, Fig. 4b). Based on these reactivity enhancements coupled with the increased asymmetry of the reactions (Table 2), we posit that adjacent TiWC surface sites are being activated for both HER and HOR

3296 | Energy Environ. Sci., 2016, 9, 3290–3301

This journal is © The Royal Society of Chemistry 2016

at low overpotentials *via* the spillover of adsorbed H^0 from highly dispersed surface Pt sites. Under this hypothesis where TiWC serves as a co-catalyst, one would anticipate an overall increase in the observed HOR/HER activation energy considering that unmodified TiWC is orders of magnitude less active than native Pt.

Indeed, Pt is noteworthy for its exceptionally low activation energy (E_a) of 16 kJ mol^{-1} for HOR/HER in acidic media.[20] For comparison, Pd has an activation energy of 31 kJ mol^{-1},[20] while WC has an activation energy of 45 kJ mol^{-1}.[35,36] Varying the temperature from 10 °C to 40 °C, we obtained an activation energy of 26.6 kJ mol^{-1} for the optimal 0.25 ML Pt/TiWC catalyst (Fig. 5) using the following equation:

$$\frac{\partial \log(j_0)}{\partial\left(\frac{1}{T}\right)} = -\frac{E_a}{2.303 \cdot R}$$

While we cannot completely rule out highly active and undercoordinated Pt sites as the cause for improved activity, the increased charge transfer asymmetry and the higher apparent activation energy offer strong evidence in favor of a bifunctional catalyst where TiWC actively participates in both HER and HOR. Despite this activation energy increase, the factor of 13 enhancement in Pt mass activity indicates that sub-monolayer core–shell nanoparticles offer a new route for substantial reductions in Pt loadings in both water electrolyzers and hydrogen fuel cells.

Comparison with thin film studies

Recently, the HER performance of WC and Mo_2C thin films coated with varying monolayer coverages of Pt and Pd *via* physical vapor deposition was studied in acidic media.[28–30] It was demonstrated that the activity of TMC thin films rapidly improves with monolayer coverage and levels off near the activity of the native Pt and Pd foils with just a single ML of the NM. Increasing the coverage beyond a single ML did not improve the activity, even up to 30 MLs.

With the development of a fabrication method for core–shell TMC–NM nanostructures, we can now examine structure-sensitivity differences between model catalysts and their commercially-relevant nanoscale counterparts. Fig. 6 compares the effect of varying ML coverages of Pt on the reactivity improvement for TiWC nanoparticles observed in this work and WC thin films reported previously.[28] Despite ultralow loadings of *ca.* 50 μg_{metal} cm$_{geo}^{-2}$, the supported 20 wt% TiWC/C and 20 wt% Pt/C nanoparticle catalysts outperform their bulk counterparts by 1 and 2 orders of magnitude, respectively. For the model thin films, it requires greater than *ca.* 0.7 ML Pt/WC to achieve an HER activity comparable to Pt foil. By contrast, a 0.25 ML Pt coverage in the sub-monolayer core–shell nanoparticle formulation is sufficient to achieve comparable activity to 20 wt% Pt/C. Although the effect could be attributed to easier activation of high index TiWC edge sites, it could also originate from the differing surface concentrations of adjacent Pt-WC sites. For instance, a 0.25 ML Pt/WC thin film will have large contiguous sections of both bare WC sites and Pt sites surrounded only by Pt, while the nanoparticle formulation would have the highest
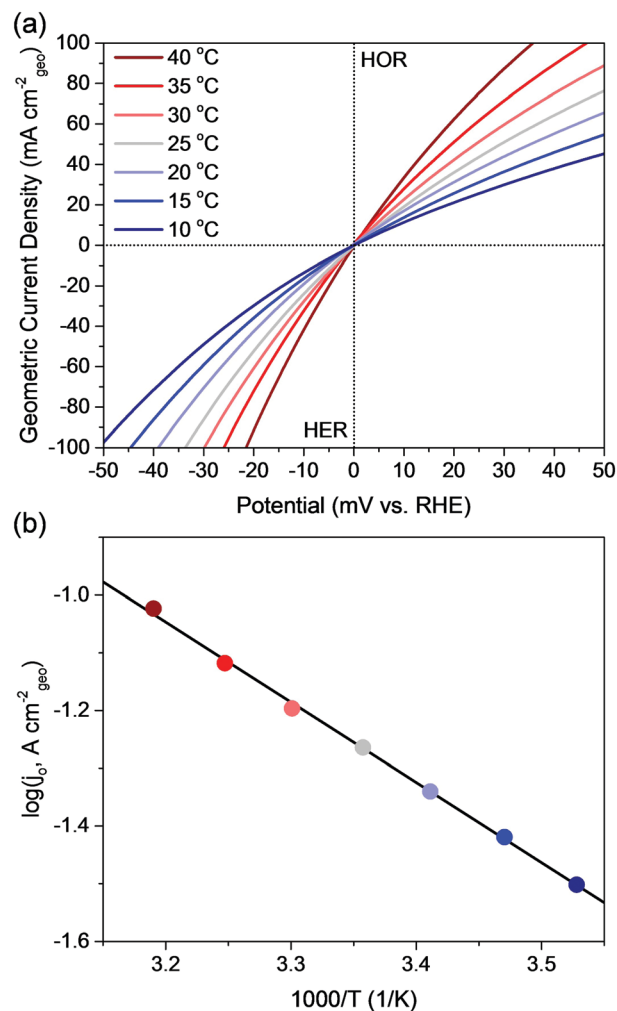

Fig. 5 (a) LSVs and (b) plot of log(j_0) *vs.* 1000/T obtained for 0.25 ML Pt/TiWC catalyst in 1.0 M $HClO_4$ at 10 mV s^{-1} at varying temperatures (10–40 °C).

intrinsic surface density of Pt sites with adjacent WC sites. For the latter case, such an arrangement would enable efficient spillover to occur at lower ML coverages than in model thin films.

Long-term durability of sub-monolayer Pt/TiWC core–shell nanoparticles

Two studies were performed on the optimal carbon-supported 0.25 ML Pt/TiWC catalyst to assess long term stability. The first study was an accelerated degradation test where the catalyst was subjected to 10 000 cycles at 100 mV s^{-1} between −50 mV and +600 mV in Ar-saturated 1.0 M $HClO_4$ using an Ag/AgCl reference electrode and a graphite rod counterelectrode. Uncompensated LSVs at 10 mV s^{-1} were collected before and afterwards in fresh electrolyte at 30 °C (Fig. 7a). In the second study (Fig. 7b), chronopotentiometry (CP) was used to examine stability under sustained, aggressive turnover. Over 16 h, the potential was allowed to vary freely to sustain HOR currents of 5 mA cm$_{geo}^{-2}$ for 15 min intervals followed by HER currents of −5 mA cm$_{geo}^{-2}$ for 15 min intervals. The open circuit voltage
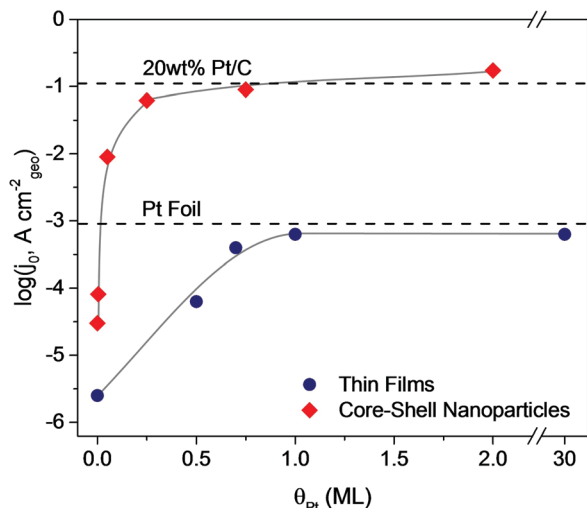
Fig. 6 Effect of Pt coverage (θ_{Pt}) on the HER activity of core−shell Pt/TiWC supported catalysts used in this work in comparison with the WC thin film study reported previously.[28]

(OCV) was determined before and after measurement to correct for any reference electrode drift. Based on the electrode mass loadings, this study involved over 140 000 turnovers on a mol H_2 mol^{-1} Pt basis and 5000 turnovers on a mol H_2 mol^{-1} total metals basis. Afterwards, the electrolyte was refreshed and an LSV scan was acquired to examine if deactivation occurred over a larger potential window (Fig. 7a).

Fig. 7 shows that the 0.25 ML Pt/TiWC catalyst is highly stable. After 10 000 cycles, the catalyst did not deactivate relative to its initial activity (Fig. 7a). During sustained turnover, a *ca.* 9 mV uncompensated overpotential was required to drive 5 mA cm$_{geo}^{-2}$ of both HOR and HER current density, and no long-term drift was observed over 16 h on stream (Fig. 7b). After this turnover study, the catalyst also did not deactivate relative to its initial activity (Fig. 7a).

Technoeconomic analysis

For water electrolysis in acidic media, OER remains the critical barrier to commercialization, requiring expensive IrO_2-based electrocatalysts with large overpotentials.[37] While significant challenges persist to overcome these barriers, it also prompts the development of ultralow-cost HER cathodes to help offset overall device cost. Likewise, for proton exchange membrane fuel cells (PEMFCs), ORR remains the critical barrier to commercialization, requiring expensive Pt-based electrocatalysts with large overpotentials. Unlike OER in acidic media, impressive results have been obtained at reducing Pt loadings while simultaneously improving activity and stability for ORR.[19,38–40] These encouraging achievements should accelerate the widespread commercial adoption of PEMFCs, motivating the development of HOR electrocatalysts with even lower Pt loadings and improved CO tolerance to further offset both the device cost and hydrogen purification cost.

As a result of its high Pt mass activity for both HER and HOR as well as its high stability, sub-monolayer core–shell nanoparticles
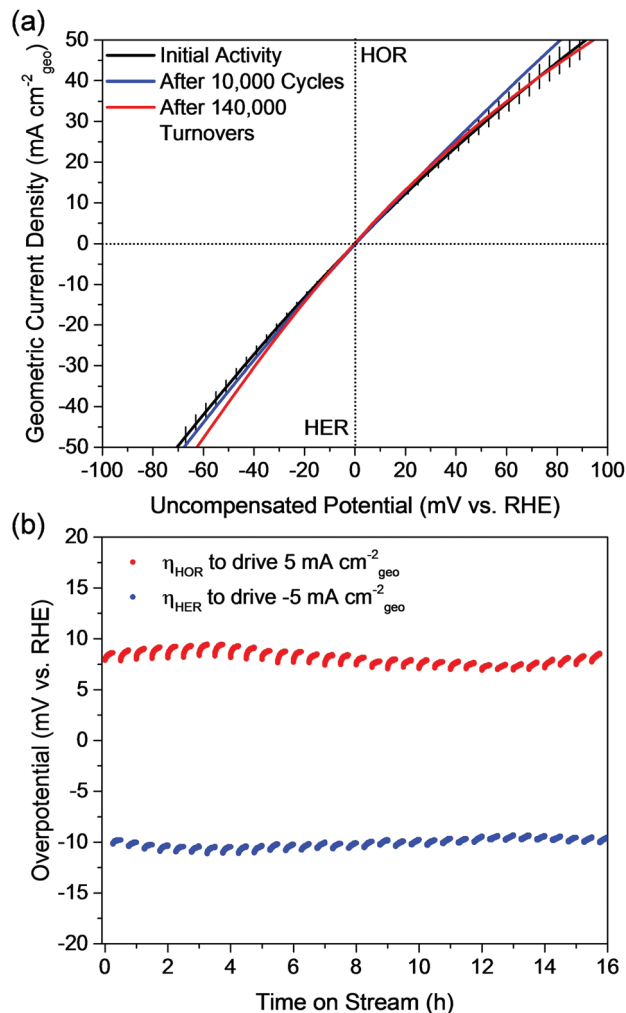

Fig. 7 (a) LSVs obtained for 0.25 ML Pt/TiWC catalyst in 1.0 M $HClO_4$ at 10 mV s^{-1} at 30 °C before and after cycling and chronopotentiometry studies. The initial activity LSVs were averaged over 5 replicate electrode mountings. (b) Chronopotentiometry studies for 0.25 ML Pt/TiWC catalyst involving over 140 000 turnovers on a mol H_2 mol^{-1} Pt basis. Cycling conditions: 10 000 cycles at 100 mV s^{-1} from −50 mV to 600 mV in 1.0 M $HClO_4$. Chronopotentiometry conditions: +5 mA cm$_{geo}^{-2}$ for 15 min followed by −5 mA cm$_{geo}^{-2}$ for 15 min for 16 h, uncompensated.

represent an exciting new direction for designing highly active and stable catalysts. Given that Pt is used in our new catalyst formulations, a technoeconomic analysis is required to understand if the cost of Pt is offset by the efficiency gains from the reduction in operating overpotentials with respect to a Pt-free alternative. The following technoeconomic analysis was performed with the goal of providing prediction intervals at 95% confidence (constructed assuming unknown means and unknown variances) for the cost reductions achievable with sub-monolayer core–shell nanoparticle formulations. This analysis was performed for both HER cathodes and HOR anodes using two economic descriptors. The first descriptor is the cost of Pt loaded. Using publicly available data that was subsequently inflation-adjusted based on the consumer price index, the average 5 year cost of Pt over 2010–2015 was calculated to be 50 ± 7 \$ g$_{Pt}^{-1}$. The second descriptor

3298 | *Energy Environ. Sci.*, 2016, **9**, 3290–3301

This journal is © The Royal Society of Chemistry 2016

is the average U.S. cost of electricity. Calculated using the same method as the Pt cost, the average 5 year cost of electricity over 2010–2015 constituted 12.5 ± 0.4 ¢ kW h^{-1}. This descriptor is used to capture the cost related to the operating overpotentials associated with HER and HOR for the various catalysts. For both HER and HOR, the overpotentials used in the analysis were the overpotentials required to drive 20 mA cm$_{geo}^{-2}$. While Pt is a capital cost based on the size of the device, the energy cost is incurred over the useful hypothetical lifecycle of the device. Therefore, the technoeconomic analysis was conducted over a 1 m^2 device with a useful lifespan of 50 000 h.

The results are shown in Fig. 8 for a cathode HER device and Fig. S5 (ESI†) for an anode HOR device. The analysis does not encompass the cost of a complete device that includes the counter electrode and membrane electrode assembly. Instead, it differentially compares multiple HER cathode and HOR anode catalysts assuming that the other device costs would be the same across all catalyst options. For HER, the materials are compared to a hypothetical earth-abundant catalyst that achieves -20 mA cm$_{geo}^{-2}$ while operating at a 100 mV overpotential, does not deactivate over the device lifetime, and has negligible materials cost. CoP is one such possible candidate, but would necessitate more rigorous stability testing and higher activity with lower loadings to meet these requirements.

It is clear from Fig. 8 that earth-abundant catalysts, such as CoP, are already capable of outperforming Pt/C even with its low 50 µg$_{Pt}$ cm$_{geo}^{-2}$ loading, provided these catalysts can remain stable over the operational lifetime of interest. This assumption results in a total cathode lifetime cost of \$127 m^{-2} for CoP as compared to \$260 m^{-2} for Pt/C. Here, the cost of CoP is entirely associated with the extra electricity (required from the catalyst overpotential) needed to power the cathode over the lifetime of the device, whereas for Pt/C, the cost of extra electricity to power the cathode accounts for less than 2% of the total cost. While Pt is expensive, perhaps more important than the price is the span of the 95% prediction interval, which ranges from \$191 m^{-2} to \$329 m^{-2}, pointing to the extreme volatility of Pt supplies. Even low loadings of 50 µg$_{Pt}$ cm$_{geo}^{-2}$ result in substantial risk exposure to Pt price volatility. By contrast, the prediction interval for CoP spans from \$119 m^{-2} to \$135 m^{-2}, a significantly smaller window due to the much lower volatility in electricity costs.

When the price risk associated with Pt is eliminated, an earth-abundant catalyst, such as CoP, only results in a factor of 2 decrease in the cost of an HER cathode, assuming that it could maintain its 100 mV overpotential at 20 mA cm$_{geo}^{-2}$. Alternatively, sub-monolayer core–shell nanoparticles offer both substantial cost savings and lower risk exposure, with the prediction interval for 0.25 ML Pt/TiWC catalyst spanning \$17 m^{-2} to \$23 m^{-2}. This value represents a factor of 12 reduction in cost as compared to 20 wt% Pt/C and a factor of 6 reduction in cost compared to CoP. For 0.25 ML Pt/TiWC, the cost of Pt accounts for 50% of the total device cost, or *ca.* \$10 m^{-2}.

While not included in the technoeconomic analysis, it is worth noting that earth-abundant catalysts currently require high loadings above *ca.* 1 mg cm$_{geo}^{-2}$. While the cost of Co and other 3d or early transition metals is small, an additional \$1–2 m^{-2} should be anticipated in the device capital costs. By contrast, the optimal 0.25 ML Pt/TiWC catalyst uses 50 µg cm$_{geo}^{-2}$ loadings of TiWC. Based on the price of W, this amounts to an additional materials cost below 0.1 ¢ m^{-2}. Moving earth-abundant catalyst loadings beyond 10 mg cm$_{geo}^{-2}$ would make the cost of the earth-abundant catalysts actually comparable to the cost of Pt in the 0.25 ML Pt/TiWC catalyst.

For HOR, the poor performance of earth-abundant alternatives would render PEMFCs inoperable without the use of prohibitively large catalyst loadings (Fig. S5, ESI†). In contrast, the price reductions associated with Pt/TiWC core–shell nanoparticles mirror closely that of the HER analysis. While these materials are asymmetric catalysts, the asymmetry of the reaction dominates at current densities above 20 mA cm$_{geo}^{-2}$ with the exception of the 0.05 ML Pt/TiWC catalyst, which requires more than 100 mV to achieve 20 mA cm$_{geo}^{-2}$. In addition to substantial opportunities for Pt reductions, it was also shown previously that the Pt/TiWC system can be used to design highly CO-tolerant electrocatalysts.[24] Currently, the CO levels in fuel cell-grade hydrogen must be rigorously maintained below 10 ppm. Reaching such low CO levels requires an extra unit operation to perform preferential oxidation (PROx), increasing fuel costs. The CO-tolerant core–shell architecture offers the opportunity to both reduce Pt loading requirements while also offering additional cost savings by loosening the constraints of the PROx process.

Comparison with other nanostructured materials

Despite critical and important efforts to standardize measurement practices,[5] it remains difficult to make meaningful comparisons between HER nanomaterials in the literature due to a lack of standardized protocols for activity and stability measurements. Oftentimes, comparisons are made from LSV data, such as that presented in Fig. 3a where the activity is gauged based on the
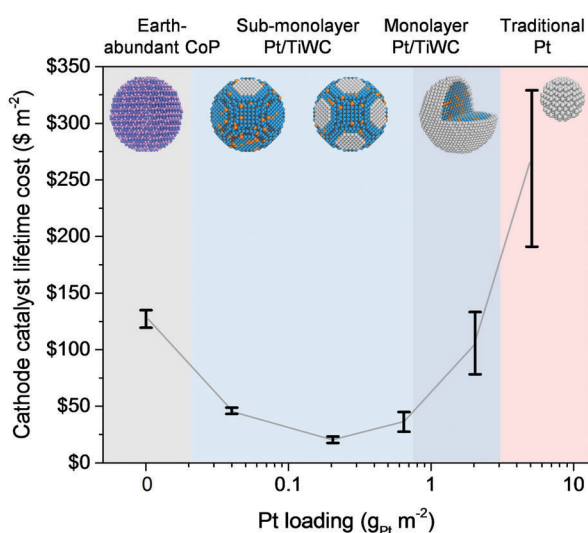

Fig. 8 Technoeconomic comparison of earth-abundant CoP catalyst with Pt-containing catalysts expressed as cathode catalyst lifetime cost *vs.* Pt loading. Error bars represent prediction intervals with 95% confidence.

This journal is © The Royal Society of Chemistry 2016

Energy Environ. Sci., 2016, **9**, 3290–3301 | **3299**

overpotential required to drive a certain geometric rate, such as -5 mA cm_{geo}^{-2}. For instance, CoP can achieve this rate with a 60 mV overpotential,[12] while TiWC requires a 280 mV overpotential (Fig. 3a). However, when comparing both values, it should be noted that CoP was loaded at 2 mg cm_{geo}^{-2} whereas TiWC was loaded at 50 μg cm_{geo}^{-2}, a factor of 40 lower. The importance of electrode mass loadings is apparent when comparing 0.15 wt% Pt/C to 20 wt% Pt/C in Fig. 3a. Clearly, reporting the electrode mass loadings is critical when reporting the performance of new electrocatalysts. While comparing catalysts on a mass basis rather than geometric activity basis is one solution, this approach is only appropriate if the catalysts are made from the same material or have similar molecular weights. Instead, a more general solution is to report exchange current densities normalized by moles of the active phase. Towards this end, we report that TiWC has an exchange current density of 109 A mol_{TiWC}^{-1} when measured in 1.0 M $HClO_4$ at 30 °C under an H_2 partial pressure of 101.3 kPa.

A second option is to compare developed materials to a Pt standard measured under identical conditions, which has been a successful strategy in the ORR literature. In this respect, it is important to define the exact nature of the standard. For instance, it is common to use a low-surface area Pt wire rather than state-of-the-art commercial Pt/C catalysts as a control. Low-surface area Pt is not an appropriate control for earth-abundant nanomaterials, as can be seen in Fig. 6 where 20 wt% Pt/C is *ca.* 100 times more active than a Pt foil. Importantly, the intrinsic activity of Pt towards HER is so high that it cannot be measured accurately with a stationary electrode or even a rotating disk electrode (RDE). Instead, HER measurements involving Pt require H_2-pump experiments or GDE measurements are needed to extract intrinsic kinetics in the absence of mass transfer limitations. Using GDEs, we report that 20 wt% Pt/C requires less than a 1 mV overpotential (iR-compensated) to drive -5 mA cm_{geo}^{-2} in 1.0 M $HClO_4$ at 30 °C under an H_2 partial pressure of 101.3 kPa when loaded at 51 $μg_{Pt}$ cm_{geo}^{-2}.

Lastly, the design of earth-abundant HER electrocatalysts has advanced to a level where it is arguably more important to achieve stability improvements rather than raw activity improvements. New earth-abundant catalyst designs should be subjected to more than 10 000 cycles over wide potential windows, with anodic potentials that better simulate degradation conditions in the fuel cell assembly (*e.g.* +500 mV). Designing anodically stable earth-abundant electrocatalysts are critical to the development of HOR co-catalysts. As such, we demonstrated stability over 10 000 cycles and up to +600 mV with stability maintained over 100 000+ turnovers. Lastly, we emphasize the importance of avoiding the use of Pt counterelectrodes during stability studies in order to prevent Pt dissolution during OER and subsequent cathodic deposition onto the working electrode.[34]

Conclusions

We developed a catalyst design platform whereby the extraordinarily high activity of Pt is harnessed to activate earth-abundant transition metal carbide nanoparticles for both HER and HOR *via* a sub-monolayer core–shell configuration. This avenue opens the possibility of reducing the already low Pt loadings needed to efficiently perform HER and HOR by an order of magnitude, to levels that can be considered negligible in terms of overall device cost. TiWC nanoparticles were shown to be ideal core candidates for supporting sub-monolayer amounts of Pt, capable of withstanding 10 000 cycles between -50 and $+600$ mV as well as over 140 000 turnovers. In comparison with prior thin film monolayer Pt/WC studies, it was observed that core–shell nanoparticles require significantly lower monolayer coverages to approach the activity of Pt nanoparticles, with 0.25 ML offering the highest Pt mass activity. A technoeconomic analysis reveals that such sub-monolayer core–shell nanoparticles could offer a factor of 12 reduction in catalyst costs compared to state-of-the-art Pt/C and a factor of 6 reduction in energy costs compared to the best earth-abundant electrocatalysts developed to date. Sub-monolayer Pt configurations could be applied to other earth-abundant ceramic cores, such as phosphides and sulfides, to further improve activity while also potentially imparting HOR activity.

Acknowledgements

Notes and references

1 N. S. Lewis and D. G. Nocera, *Proc. Natl. Acad. Sci. U. S. A.*, 2006, **103**, 15729.
2 K. Sasaki, H. Naohara, Y. Choi, Y. Cai, W. F. Chen, P. Liu and R. R. Adzic, *Nat. Commun.*, 2012, **3**, 1115.
3 R. T. Atanasoski, L. L. Atankasoska and D. A. Cullen, in *Electrocatalysis in Fuel Cells: A Non- and Low-Platinum Approach*, ed. M. Shao, Springer, London, 2013, p. 637.
4 S. Shrestha and W. E. Mustain, in *Electrocatalysis in Fuel Cells: a Non- and Low- Platinum Approach*, ed. M. Shao, Springer, London, 2013, p. 689.
5 C. C. McCrory, S. Jung, I. M. Ferrer, S. M. Chatman, J. C. Peters and T. F. Jaramillo, *J. Am. Chem. Soc.*, 2015, **137**, 4347.
6 W. Sheng, A. P. Bivens, M. Myint, Z. Zhuang, R. V. Forest, Q. Fang, J. G. Chen and Y. Yan, *Energy Environ. Sci.*, 2014, **7**, 1719.
7 K. Gong, F. Du, Z. Xia, M. Durstock and L. Dai, *Science*, 2009, **323**, 760.
8 Y. Liang, Y. Li, H. Wang, J. Zhou, J. Wang, T. Regier and H. Dai, *Nat. Mater.*, 2011, **10**, 780.
9 W. Sheng, H. A. Gasteiger and Y. Shao-Horn, *J. Electrochem. Soc.*, 2010, **157**, B1529.
10 H. T. Duong, M. A. Rigsby, W.-P. Zhou and A. Wieckowski, *J. Phys. Chem. C*, 2007, **111**, 13460.

3300 | *Energy Environ. Sci.*, 2016, **9**, 3290–3301

This journal is © The Royal Society of Chemistry 2016

11 T. Xu, *J. Membr. Sci.*, 2005, **263**, 1.

12 E. J. Popczun, C. G. Read, C. W. Roske, N. S. Lewis and R. E. Schaak, *Angew. Chem., Int. Ed.*, 2014, **53**, 5427.

13 M. Caban-Acevedo, M. L. Stone, J. R. Schmidt, J. G. Thomas, Q. Ding, H.-C. Chang, M.-L. Tsai, J.-H. He and S. Jin, *Nat. Mater.*, 2015, **14**, 1245.

14 M. S. Faber, R. Dziedzic, M. A. Lukowski, N. S. Kaiser, Q. Ding and S. Jin, *J. Am. Chem. Soc.*, 2014, **136**, 10053.

15 P. Jiang, Q. Liu, Y. Liang, J. Tian, A. M. Asiri and X. Sun, *Angew. Chem., Int. Ed.*, 2014, **53**, 12855.

16 E. J. Popczun, J. R. McKone, C. G. Read, A. J. Biacchi, A. M. Wiltrout, N. S. Lewis and R. E. Schaak, *J. Am. Chem. Soc.*, 2013, **135**, 9267.

17 J. X. Wang, Y. Zhang, C. B. Capuano and K. E. Ayers, *Sci. Rep.*, 2015, **5**, 1.

18 K. Elbert, J. Hu, Z. Ma, Y. Zhang, G. Chen, W. An, P. Liu, H. S. Isaacs, R. R. Adzic and J. X. Wang, *ACS Catal.*, 2015, **5**, 6764.

19 C. Chen, Y. Kang, Z. Huo, Z. Zhu, W. Huang, H. L. Xin, J. D. Snyder, D. Li, J. A. Herron, M. Mavrikakis, M. Chi, K. L. More, Y. Li, N. M. Markovic, G. A. Somorjai, P. Yang and V. R. Stamenkovic, *Science*, 2014, **343**, 1339.

20 J. Durst, C. Simon, F. Hasche and H. A. Gasteiger, *J. Electrochem. Soc.*, 2014, **162**, F190.

21 H. Yang, *Angew. Chem., Int. Ed.*, 2011, **50**, 2674.

22 D. V. Esposito and J. G. Chen, *Energy Environ. Sci.*, 2011, **4**, 3900.

23 I. E. Stephens, A. S. Bondarenko, U. Grønbjerg, J. Rossmeisl and I. Chorkendorff, *Energy Environ. Sci.*, 2012, **5**, 6744.

24 S. T. Hunt, M. Milina, A. C. Alba-Rubio, C. H. Hendon, J. A. Dumesic and Y. Roman-Leshkov, *Science*, 2016, **352**, 974.

25 S. T. Hunt, T. Nimmanwudipong and Y. Roman-Leshkov, *Angew. Chem., Int. Ed.*, 2014, **53**, 5131.

26 Y. C. Kimmel, X. Xu, W. Yu, X. Yang and J. G. Chen, *ACS Catal.*, 2014, **4**, 1558.

27 S. T. Hunt, T. M. Kokumai, D. Zanchet and Y. Roman-Leshkov, *J. Phys. Chem. C*, 2015, **119**, 13691.

28 D. V. Esposito, S. T. Hunt, A. L. Stottlemyer, K. D. Dobson, B. E. McCandless, R. W. Birkmire and J. G. Chen, *Angew. Chem., Int. Ed.*, 2010, **49**, 9859.

29 D. V. Esposito, S. T. Hunt, Y. C. Kimmel and J. G. Chen, *J. Am. Chem. Soc.*, 2012, **134**, 3025.

30 T. G. Kelly, S. T. Hunt, D. V. Esposito and J. G. Chen, *Int. J. Hydrogen Energy*, 2013, **38**, 5638.

31 G. Chen, S. R. Bare and T. E. Mallouk, *J. Electrochem. Soc.*, 2002, **149**, A1092.

32 S. T. Hunt and Y. Roman-Leshkov, *J. Visualized Exp.*, 2015, e53147.

33 S. H. Joo, S. J. Choi, I. Oh, J. Kwak, Z. Liu, O. Terasaki and R. Ryoo, *Nature*, 2001, **412**, 169.

34 G. Dong, M. Fang, H. Wang, S. Yip, H.-Y. Cheung, F. Wang, C.-Y. Wong, S. T. Chu and J. C. Ho, *J. Mater. Chem. A*, 2015, **3**, 13080.

35 H. Zheng, J. Huang, W. Wang and C. Ma, *Electrochem. Commun.*, 2005, **7**, 1045.

36 C. Ma, J. Sheng, N. Brandon, C. Zhan and G. Li, *Int. J. Hydrogen Energy*, 2007, **32**, 2824.

37 C. C. L. McCrory, S. Jung, J. C. Peters and T. F. Jaramillo, *J. Am. Chem. Soc.*, 2013, **135**, 16977.

38 D. Wang, H. L. Xin, R. Hovden, H. Wang, Y. Yu, D. A. Muller, F. J. DiSalvo and H. D. Abruña, *Nat. Mater.*, 2013, **12**, 81.

39 X. Huang, Z. Zhao, L. Cao, Y. Chen, E. Zhu, Z. Lin, M. Li, A. Yan, A. Zettl, Y. M. Wang, X. Duan, T. Mueller and Y. Huang, *Science*, 2015, **348**, 1230.

40 L. Zhang, L. T. Roling, X. Wang, M. Vara, M. Chi, J. Liu, S.-I. Choi, J. Park, J. A. Herron, Z. Xie, M. Mavrikakis and Y. Xia, *Science*, 2015, **349**, 412.

This journal is © The Royal Society of Chemistry 2016

Energy Environ. Sci., 2016, **9**, 3290–3301 | 3301